TU Delft

Delft University of Technology

Probing Cation Displacements in Antiferroelectrics

A Joint NMR and TEM Approach

Ding, Hui; Egert, Sonja; Huang, Binxiang; Jiang, Tianshu; Carstensen, Leif; Šić, Edina; Liu, Yucheng; Yang, Tongqing; Groszewicz, Pedro Braga; More Authors

DOI
10.1021/acs.chemmater.3c02045

Publication date
2023

Document Version
Final published version

Published in
Chemistry of Materials

Citation (APA)
Ding, H., Egert, S., Huang, B., Jiang, T., Carstensen, L., Šić, E., Liu, Y., Yang, T., Groszewicz, P. B., & More Authors (2023). Probing Cation Displacements in Antiferroelectrics: A Joint NMR and TEM Approach. *Chemistry of Materials*, *35*(23), 10041-10049. https://doi.org/10.1021/acs.chemmater.3c02045

Important note
To cite this publication, please use the final published version (if applicable).
Please check the document version above.

Copyright
Other than for strictly personal use, it is not permitted to download, forward or distribute the text or part of it, without the consent of the author(s) and/or copyright holder(s), unless the work is under an open content license such as Creative Commons.

Takedown policy
Please contact us and provide details if you believe this document breaches copyrights.
We will remove access to the work immediately and investigate your claim.

This work is downloaded from Delft University of Technology.
For technical reasons the number of authors shown on this cover page is limited to a maximum of 10.

CHEMISTRY OF MATERIALS

pubs.acs.org/cm

Article

Probing Cation Displacements in Antiferroelectrics: A Joint NMR and TEM Approach

Hui Ding,* Sonja Egert,* Binxiang Huang, Tianshu Jiang, Leif Carstensen, Edina Šić, Yucheng Liu, Tongqing Yang, Pedro Braga Groszewicz, Hans-Joachim Kleebe, Andreas Klein, Leopoldo Molina-Luna,* and Gerd Buntkowsky*

Cite This: *Chem. Mater.* 2023, 35, 10041−10049

Read Online

ACCESS | Metrics & More | Article Recommendations | Supporting Information

ABSTRACT: High-resolution scanning transmission electron microscopy (STEM) enjoys great advantages for atomic-resolution visualization of the atomic structure, while failing to disclose structural information along the atomic columns. On the other hand, solid-state nuclear magnetic resonance (NMR) spectroscopy is highly sensitive to the three-dimensional, local structure around atoms in the bulk sample but typically cannot provide an intuitive visualization of the structure. Thus, the combination of atomic-resolution (S)TEM and solid-state NMR spectroscopy has the potential to establish an in-depth, multidimensional structural understanding. Here, we explore this novel strategy to probe the structure of antiferroelectric perovskite oxides $PbZrO_3$ and $(Pb,La)(Zr,Sn,Ti)O_3$. We combine complementary information regarding the in-plane displacement vector mapping from STEM with the analysis of local PbO_{12} environments from ^{207}Pb NMR spectroscopy to provide unprecedented insight into Pb displacements. For $PbZrO_3$, an ordered 4-fold in-plane displacement modulation is clearly revealed via STEM imaging; meanwhile, the out-of-plane information is provided by two discrete ^{207}Pb NMR signals attributed to two crystallographic Pb sites in the 2D-PASS NMR spectrum. In the chemically modified $(Pb,La)(Zr,Sn,Ti)O_3$ system, disorder of the structure manifests in not only an inhomogeneous displacement modulation but also a broad distribution of ^{207}Pb chemical shifts, related to significant disorder of displacement magnitudes and a favoring of larger displacements. We show that the displacement distribution depends on whether both in-plane and out-of-plane displacements or only out-of-plane displacements are considered. Our findings demonstrate the advantages in the structural analysis using combined TEM and NMR approaches, hence laying the foundation work for controlling and optimizing functional properties.

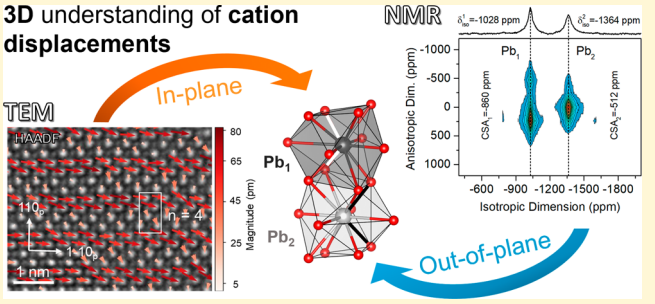

Downloaded via TU DELFT on December 20, 2023 at 10:46:53 (UTC).
See https://pubs.acs.org/sharingguidelines for options on how to legitimately share published articles.

1. INTRODUCTION

For wide range of cutting-edge applications, functional materials are on the forefront of research. An in-depth understanding of structure−property relationships is vital for optimizing material functionalities to meet modern demands. One major structural influence on the properties of materials is the displacement of cations in the lattice. Cation displacements affect, for example, structure−emission relationships and carrier mobilities in halide perovskite materials for optoelectronics,[1,2] band gaps in photovoltaics,[3] and the dielectric properties of multiferroic oxides.[4−6] In the family of antiferroelectrics, cation displacements are a main contributor to the macroscopic polarization, defining the material functionality via the switching behavior under applied electric fields.[7] However, the comprehensive characterization of cation displacements in polycrystalline materials can be challenging due to the minute distortions they impose on the structure, especially in the presence of short-range structural disorder.

During the past decades, high-resolution (scanning) transmission electron microscopy (STEM) has been widely employed in the visualization of the cation displacement mapping.[8−12] For instance, Jia et al. have mapped cation positions on the unit cell scale and observed that spontaneous polarization may not necessarily scale with tetragonality in ultrathin ferroelectric films.[11] Despite the development of advanced techniques, (S)TEM largely remains a two-dimensional imaging technique, which means that abundant information on the atomic structure out-of-plane remains unexplored. On the other hand, solid-state NMR spectroscopy is highly sensitive toward the immediate surroundings of probe nuclei in bulk samples in all three dimensions. The positions, line shapes, and line widths of NMR signals originate from nuclear spin interactions with typically short interaction ranges.

Received: August 14, 2023
Revised: November 1, 2023
Accepted: November 1, 2023
Published: November 17, 2023

ACS Publications

© 2023 American Chemical Society

Thus, NMR signals reflect the variety of direct or next-nearest neighbors, bond lengths, and angles as well as the symmetry of the local atomic environment. This makes the method notably powerful when the short-range order of the structure significantly differs from the long-range order.[13] For this reason, solid-state NMR spectroscopic studies have in the past lent important contributions to the elucidation of structure−property relations in perovskite oxides including ferroelectrics (FE),[14−16] antiferroelectrics (AFE),[17−20] and relaxor ferroelectrics.[21−25] However, to provide a visual model of the structure of complex systems, NMR spectroscopy commonly relies on the use of model systems or complementary computational methods.[26,27] A combination of (S)TEM imaging and NMR spectroscopy thus has the potential to not only provide an intuitive visualization of the atomic structure but also establish a more generalized, in-depth understanding of the three-dimensional structure.

To put a combined approach into action and maximize the advantages of both methods, the antiferroelectric (AFE) perovskites $PbZrO_3$(PZ) and $(Pb,La)(Zr,Sn,Ti)O_3$ are chosen for investigation. PZ-based AFE oxides have recently gathered interest due to their great potential for the application in high-energy-density capacitors,[28] pulse power capacitors,[29] and solid-state electrocaloric cooling systems.[30,31] While both materials are well-studied and PZ is even considered a "prototype" AFE, the relationships between local-scale Pb environments and macroscopic Pb displacement patterns remain underexplored. Local-scale information obtained from NMR spectroscopy can bridge the gap between the macroscopic properties, the long-range structure obtained from X-ray diffraction (XRD), and the cation displacement configuration. HR-(S)TEM imaging techniques are regarded as a routine approach to visualize the displacement configuration of (anti)ferroelectric materials.[32−37] However, displacement patterns resolved by (S)TEM imaging fail to distinguish the individual atoms parallel to the incident electron beam. Diffraction studies have shown that the crystal structure of AFE PZ (space group no. 55, *Pbam*) features not only the antiparallel in-plane displacements of Pb along the $[110]_p$ direction, as shown in Figure 1a, but also two crystallographic Pb sites in successive planes perpendicular to the $[110]_p$ direction (out-of-plane), denoted by Pb_1 and Pb_2 as shown in Figure 1b.[38] Although Pb_1 and Pb_2 both follow the same pattern of displacement configuration that contributes to the AFE ordering, they possess slight differences with respect to the bond lengths and covalence of Pb−O bonds as well as the magnitude of displacements, which are the greatest along the $[1\text{-}10]_p$ direction of the lattice and amount to 0.29−0.30 Å for Pb_1 and 0.26 Å for Pb_2 at low temperature.[38] This allows for these two sites to be distinguished,[38,39] which is beyond the capability of (S)TEM imaging. Instead, (S)TEM methods represent columns of alternating Pb_1 and Pb_2 and fail to assign Pb_1 and Pb_2 individually.

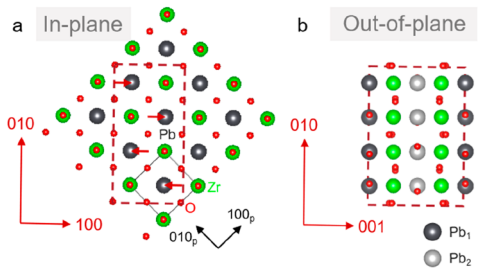

Figure 1. Schematic illustrating the structure of *Pbam* PZ at room temperature. (a) The unit cell perpendicular to the $[001]_p$ direction where the lead displacements are antiparallel in pairs perpendicular to the cubic $[110]_p$ direction. (b) The unit cell along the $[001]_p$ direction, where two Pb ion positions are identified as Pb_1 and Pb_2 given in two colors.

To resolve the Pb atoms with distinct out-of-plane displacements, ^{207}Pb solid-state NMR spectroscopy has previously shown great advantages.[40−42] While the differences between the two crystallographic sites are small, ^{207}Pb NMR spectroscopy is particularly sensitive to minute differences in Pb−O distances and hence capable to distinguish them as two well-resolved ^{207}Pb NMR signals. Their particular position, shape, and width reflect the differences in Pb−O distances, site symmetry, and deformation of the PbO_{12} environments. The characterization of spectral parameters can be significantly improved with advanced pulse sequences such as 2D-PASS,[40,43] a technique that also improves spectral resolution in chemically substituted lead-based materials, such as $(Pb,Ba)ZrO_3$.[44]

In this work, high-angle annular dark-field (HAADF) and annular bright-field (ABF) STEM imaging techniques were utilized in combination with ^{207}Pb solid-state NMR spectroscopy to probe the local atomic structure and displacement configurations of the prototype PZ and a modified AFE $(Pb_{0.97}La_{0.02})(Zr_{0.75}Sn_{0.14}Ti_{0.11})O_3$ (abbreviated PLZST) ceramic. The global structures and properties were characterized via powder X-ray diffraction and polarization-electric field hysteresis measurement, as shown in Figures S1 and S2. PLZST oxides assume a range of different AFE and FE structures as a function of their composition, the temperature, and the presence or absence of electric fields. Here, we pick a composition near the AFE-FE phase boundary as a model system with macroscopic AFE behavior but unclear displacement configuration. For PZ, we demonstrate that a 4-fold modulation of Pb displacements, expected for the crystal structure of AFE PZ, is well maintained and corroborated by two distinct Pb sites observed by NMR spectroscopy. However, the Pb displacement components within one modulation in PZ are revealed as nearly perpendicular to each other with an unequal magnitude in our investigation. In PLZST, the disorder of the structure manifests in an inhomogeneous distribution of the magnitude and orientation of the Pb displacements as well as the modulation period. This is complemented by the presence of only one ^{207}Pb NMR signal, revealing considerable disorder of Pb atoms following a distribution of displacement magnitudes. The novel combination of TEM and solid-state NMR spectroscopy opens the door to probe not only the in-plane Pb displacements but also the out-of-plane environments, deepening our understanding of antiferroelectricity in complex materials, hence paving the way for future structure−property correlation in functional materials.

2. EXPERIMENTAL SECTION

The PZ and PZ-based (PLZST) ceramics were synthesized by a ceramic processing route via the solid-state reaction using PbO (99%), La_2O_3 (99.99%), ZrO_2 (99%), SnO_2 (99.5%), and TiO_2 (98%, all Sinopharm Chemical Reagent Co., Ltd., Shanghai) as starting reagents. To compensate for the lead loss, an additional 2 wt % of PbO was added. The oxide powders were mixed in ethanol (PZ) or

https://doi.org/10.1021/acs.chemmater.3c02045
Chem. Mater. 2023, 35, 10041−10049

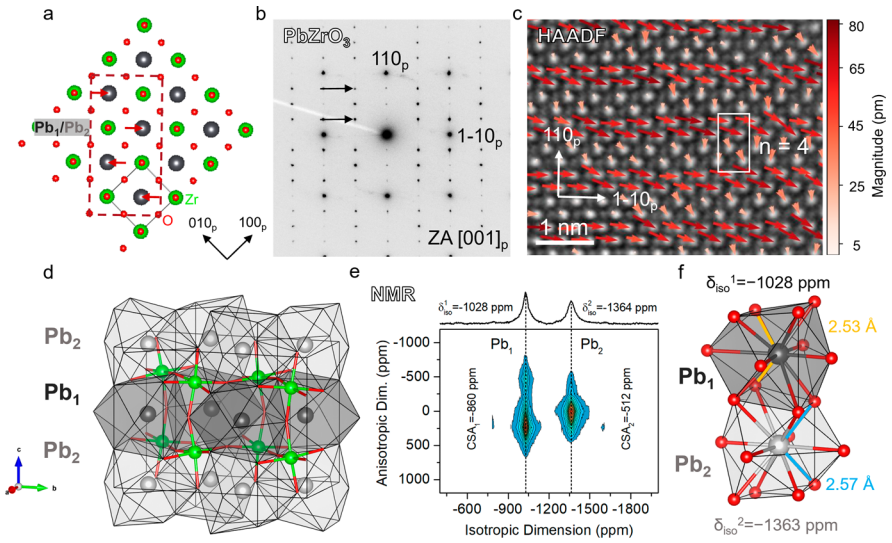

Figure 2. (a) Schematic illustration of the in-plane crystal structure of PZ, where Pb_1 and Pb_2 are overlaid. (b) SAED pattern of PZ in the $[001]_p$ zone axis with characteristic 1/4 type superlattice reflections, denoted by the black arrows. (c) Displacement vector map overlaid on the HAADF-STEM image, where a 4-fold (2 + 2) displacement pattern formulating one unit cell (white rectangle) is recognized along the $[110]_p$ direction. (d) Illustration of the unit cell with alternating layers of Pb_1 and Pb_2. (e) ^{207}Pb 2D-PASS NMR spectrum of PZ, where the direct dimension refers to the isotropic chemical shift (δ_{iso}, characteristic signal position) and the indirect dimension refers to the chemical shift anisotropy (CSA, characteristic signal width). The two distinct signals with different δ_{iso} and CSA are assigned to Pb_1 and Pb_2. (f) Illustration of the local atomic environments of Pb_1 and Pb_2, which differ with respect to the shortest Pb−O distance (depicted in color).

deionized water (PLZST) and ball milled for 24 h. For both PZ and PLZST, calcination was performed at 900 °C for 2 h, followed by a second ball-milling step. For PZ, the ball-milled powder was mixed with poly(vinyl alcohol) (PVA), pressed into a compact slip using a tape-rolling process, and then cut into small square pieces. For PLZST, the powder after a granulation step with PVA binder was directly pressed into 10 mm diameter pellets.[45] After burning off the PVA at 600 °C for 2 h (PZ) or 3 h (PLZST), the pellets were sealed in alumina crucibles and sintered at 1240 °C for 2 h (PZ) or 1250 °C for 3 h (PLZST).

The TEM samples were prepared conventionally, as described elsewhere.[46] The TEM studies were performed using a JEM 2100F microscope (JEOL, Japan) operating at 200 keV. The STEM studies were performed on a Cs-corrected JEM ARM 200F microscope (JEOL, Japan) operating at 200 keV. The STEM imaging conditions used were probe size of 8C and convergence angle of 25 mrad and a collection semiangle of 90−370 mrad for HAADF and of 11−23 mrad for ABF-STEM imaging. The center of each Pb and B site atomic column is mapped by applying the Centre of Mass and 2D-Gaussian algorithms via Atomap[47] and TEMUL Toolkit.[48] The precision of the coordinates of these centers reaches the subpixel level. The sublattice displacement of Pb with respect to the B site sublattice is calculated based on the vector between a Pb atom and the midpoint of the four nearest B site atoms. To calculate the Pb−O distance, first, the Pb and B site atomic column position in the ABF image is subtracted, and second the center of each O atomic column is mapped by removing the signal from the Pb and B site atoms using Centre of Mass and 2D-Gaussian algorithms via Atomap.[47] Knowing the positions of all the atoms, the distances between Pb and its four surrounding O atoms are calculated to obtain the average and smallest value from these four distances.

For the solid-state NMR characterization, sintered pellets were crushed to powders and subsequently annealed at 400 °C for 2 h in air to alleviate mechanical stresses in the material. ^{207}Pb solid-state NMR spectra were recorded using a Bruker Avance III spectrometer operating at a 7.1 T magnet. Experiments were performed with magic angle spinning (MAS) at a frequency of 15 kHz with a 3.2 mm MAS probe. A modified shifted-echo version of the two-dimensional phase-adjusted spinning sidebands (2D-PASS) sequence was used where the duration of one rotor period was added before and after the last π pulse.[49] Pulse lengths were 1.85 μs for the initial $\pi/2$ pulse and 5.8 μs for the subsequent five π pulses. 16-pitch experiments were performed with 1458 transients averaged on each pitch and a recycle delay of 10 s.[50] ^{207}Pb chemical shifts were referenced to the Pb_2 signal of PZ (99.997%, Alfa Aesar, Germany) at −1363 ppm (Figure S3).[51] Purely isotropic projections of the spectra were obtained by summation along the direct axis after a shearing operation along the diagonal axis while chemical shift anisotropy (CSA) patterns were extracted as slices along the indirect axis. Line shape simulations of CSA patterns were performed with the program DMFit.[52] CSA values are reported according to the conventions provided in the Supporting Information.

3. RESULTS AND DISCUSSION

3.1. Combined 3-Dimensional Characterization of PZ.

The schematic crystal structure and crystallography of the PZ ceramic are shown in Figure 2a,b, where characteristic 1/4 superlattice reflections along the $[110]_p$ direction are marked by the black arrows. It is known that the displacement of Pb atoms is almost three times that of Zr atoms;[53] thus, it is reasonable to calculate the relative displacement of Pb with respect to the geometric center of the four surrounding Zr atoms columns.[33,34] The displacement vector map is overlaid on the HAADF-STEM image, displayed in Figure 2c. In the inset HAADF-STEM image shown in Figure 2c, the Pb and Zr atoms can easily be identified due to their significant difference in atomic number. The atomic structure of cubic PZ is overlaid to the inset image for better visualization. Clearly, a 4-fold (2 + 2) displacement modulation formulating one unit cell along the $[110]_p$ direction is observed, consistent with the 4-fold nature of the crystal structure of PZ. However, the displacement of Pb atoms is neither fully antiparallel nor compensated in the magnitude, contrasting the well-accepted Kittel model.[54] The unanticipated configuration was also observed in another domain oriented in the same zone axis, for which the STEM imaging processing involved both rigid and nonrigid image registration to minimize the artifacts introduced during data acquisition (Figure S4). Indeed, such uncompensated polar-

https://doi.org/10.1021/acs.chemmater.3c02045
Chem. Mater. 2023, 35, 10041−10049

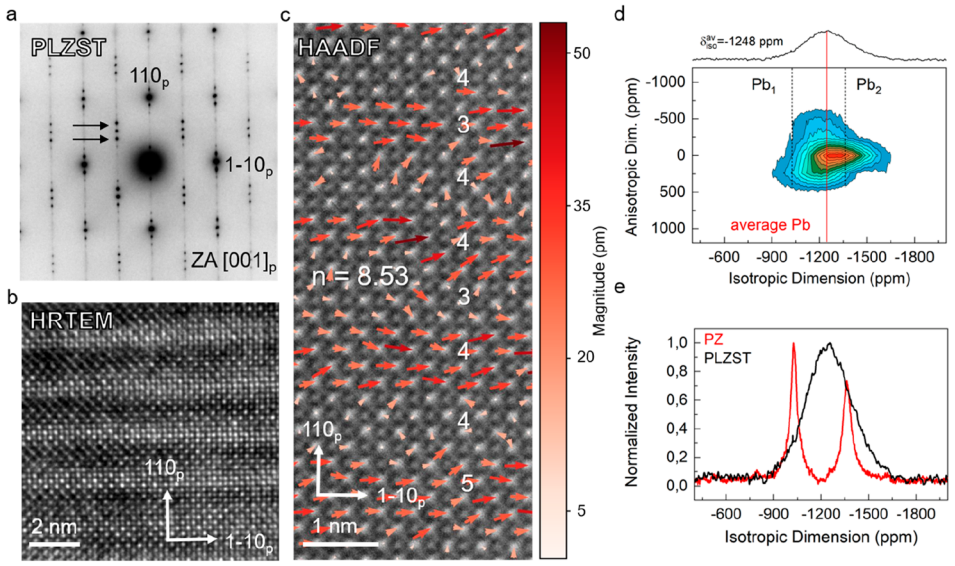

Figure 3. (a) SAED pattern of PLZST in the $[001]_p$ zone axis, characterized by the satellites along the [110] direction marked by the black arrows. (b) HRTEM image demonstrating the modulated structure. (c) Displacement vector map overlaid on the HAADF-STEM image, revealing a mixed 7 (3 + 4), 8 (4 + 4), and 9 (4 + 5)-fold modulated displacement pattern in-plane along the $[110]_p$ direction. (d) Sheared ^{207}Pb 2D-PASS spectrum of PLZST indicating an averaged local environment with a broad parameter distribution and significant disorder of the Pb displacement magnitudes in the PbO_{12} coordination spheres. The positions of the Pb_1 and Pb_2 signals in PZ are included as a visual guide. (e) Purely isotropic projection of the 2D-PASS spectrum depicting the distribution of isotropic chemical shifts in PLZST.

ization has been frequently observed in lead-based antiferroelectrics,[34,55,56] and the systems are usually attributed to the ferrielectricity group.[33,57] The ferrielectric state is assumed to be an intermediate state between antiferroelectric and ferroelectric ordering,[34] bridging the AFE to FE phase transformation.[56] Given that modifications of the displacement configuration away from the classic view of PZ have been reported,[55,57] it is concluded that on a local scale PZ may not be ideally antiferroelectric at room temperature but bears an uncompensated polarization instead. On the other hand, this finding can be regarded as experimental observation with respect to the speculation from Rabe[58] that PZ cannot be described by two sublattices with opposite polarization. Nevertheless, comparative theoretical studies of the free energy are expected to determine the stability of such a configuration at room temperature.

To enhance the understanding of the Pb displacement configuration in PZ, ^{207}Pb NMR spectroscopy is employed for probing out-of-plane differences between the Pb_1 and Pb_2 sites (Figure 2d). The ^{207}Pb 2D-PASS spectrum of PZ after a shearing operation[50] is displayed in Figure 2e. The 2D-PASS sequence allows for the signals corresponding to Pb_1 and Pb_2 to be separated in a two-dimensional array where the direct dimension corresponds to the isotropic chemical shift (δ_{iso}, characteristic signal position) and the indirect dimension corresponds to the chemical shift anisotropy (CSA, characteristic signal width). While δ_{iso} is a quantity highly sensitive to the Pb−O bond lengths, the CSA is related to the symmetry of the PbO_{12} coordination sphere and the covalency of Pb−O bonds.[21,39,43] Both parameters can be determined by line shape fitting.[22,40,51,59] Figure 2e exhibits two signals with $\delta_{iso,1}$ = −1028 ± 0.1 ppm and $\delta_{iso,2}$ = −1364 ± 0.2 ppm as well as CSA_1 = −860 ± 25 ppm and CSA_2 = −512 ± 15 ppm, indicating two crystallographic sites with slightly different atomic environments (Figure 2f).

Quantitative comparisons between the local structure and the average crystal structure can be performed employing the following empirical relation between ^{207}Pb isotropic chemical shifts δ_{iso} and Pb−O bond lengths r_{Pb-O}, which is recalled in detail in the Supporting Information:[59−61]

$$\delta_{iso}\ (\text{ppm}) = 20854 - 8669 r_{Pb-O}\ (\text{Å}) \quad (1)$$

For PZ, the calculation of r_{Pb-O} from δ_{iso} yields values of approximately 2.52 and 2.56 Å for Pb_1 and Pb_2, respectively. These values are in agreement with the shortest Pb−O distances of the two sites according to the crystal structure, which amount to 2.53 and 2.57 Å and are depicted in Figure 2f.[38] Hence, the quantity r_{Pb-O} is termed the *effective bond length* to highlight that due to variations in the 12 surrounding Pb−O bond lengths, they do not contribute equally to an arithmetic mean in the relation between average isotropic chemical shift and Pb−O bond lengths calculated from it. Instead, we can assume that this average is dominated by the shortest bond (in-plane and out-of-plane) present in the structure.[44,59,60] Additionally, Pb_1−O bonds are known to be more covalent along the ⟨100⟩ direction,[38,39] which is in accordance with the larger CSA for the Pb_1 site. Both CSA values indicate bonding environments midway between typical covalent and ionic,[40,60] which agrees with the off-center Pb atoms forming covalent bonds only with their closest oxygen neighbors.[62,63] Based on these comparisons, it is evident that ^{207}Pb NMR spectroscopy is highly sensitive to Pb−O bonding. The extracted data are consistent with the average structure reported from diffraction studies, and NMR data consistent with our analysis of PZ have previously been reported.[40−42] Furthermore, the sharp, well-resolved signals indicate that any structural disorder present in our sample occurs on a much smaller scale than the differences between the two crystallographic sites.[44,59,60] While disorder may exist on a local scale, most of the sample is thus well-described by the ordered average structure. This result is in accordance with a previous

https://doi.org/10.1021/acs.chemmater.3c02045
Chem. Mater. 2023, 35, 10041−10049

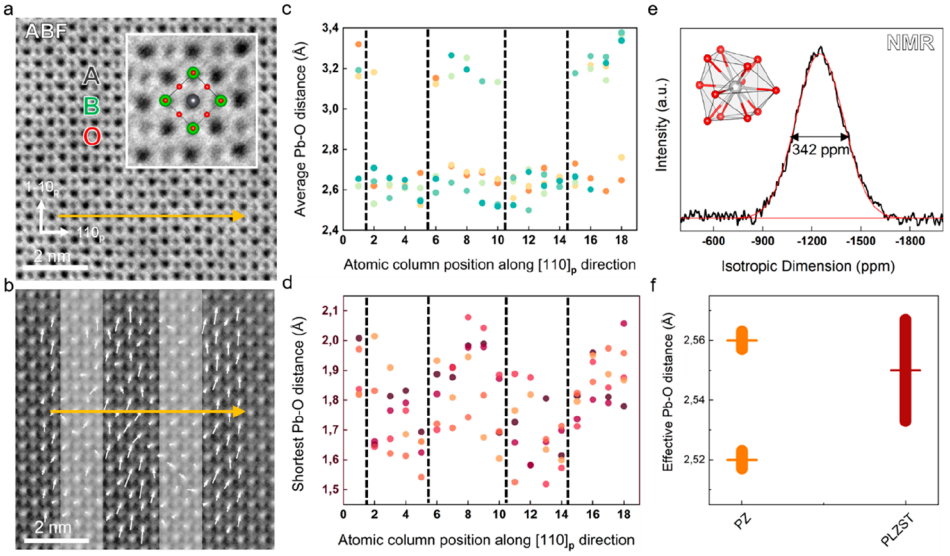

Figure 4. (a) Rotated ABF image of PLZS with the $[110]_p$ direction being horizontal for the convenience of the calculation of the Pb−O distance. (b) Displacement vector map overlaid on the ABF image. (c, d). The average and the shortest Pb−O distance over several planes along the $[1-10]_p$ direction with respect to the atomic column position along the $[110]_p$ direction as indicated by the orange arrow in (b). The dashed black lines separate the components with different magnitudes in the displacement map b. (e) Simulation of the purely isotropic projection obtained from the 2D-PASS spectrum of PLZST fitted with a Gaussian function. The FWHM of the curve is 342 ± 1 ppm (standard deviation: 145 ppm). (f) Effective Pb−O distance calculated from the distribution of isotropic chemical shifts in the NMR spectra, as reflected in the FWHM of the signals.

^{207}Pb NMR study which obtained sharp powder line shapes, indicating no random deviations from orthorhombic symmetry and no random Pb displacements in PZ.[64] It also supports our assumption that the deviations from the expected polarization configuration that we have observed with STEM are of a purely local nature as well as additional confirmation that our sample of PZ exhibits the expected crystal structure.

3.2. Combined 3-Dimensional Characterization of PLSZT. With the knowledge of the displacement arrangement in the benchmark material PZ, we apply this methodology to examine the antiferroelectricity in PLZST, as illustrated in Figure 3. $(Pb_{0.97}La_{0.02})(Zr_{0.75}Sn_{0.14}Ti_{0.11})O_3$ serves as a model composition for the PLZST system close to the AFE-FE phase boundary. The crystallography of the PLZST ceramic is shown in Figure 3a. Characteristic incommensurate (ICM) type satellites are observed in the SAED pattern, which is, in fact, an average effect arising from an ensemble of commensurate modulations with different modulation lengths.[65,66] In this case, the modulation period of the ICM satellites is calculated to be n = 8.53, as derived from the position of the satellites between the two main reflections. Note that n is integer with value 4 in PZ. The modulated structure resolved by high-resolution TEM (HRTEM) in Figure 3b is further characterized by the HAADF-STEM, overlaid with the displacement vector map in Figure 3e. Each modulation features two components with significantly different magnitudes. The one with the larger magnitude is nearly parallel to the $[1\text{-}10]_p$ direction while the one with smaller magnitude is oriented in a disordered fashion. Such highly disordered displacement has been argued to be a modulated AFE state that facilitates the electric-field-induced AFE-to-FE transformation as an intermediate bridge.[56] Moreover, an inhomogeneous distribution of the modulation period is readily seen, with values of 7, 8, and 9, resulting in the average value of 8.53 that was calculated. In short, the atomistic findings demonstrate a vigorous disorder of Pb positions as shown by the inhomogeneous modulation of the displacement configuration in-plane as compared to the rigid, 4-fold modulation of PZ. Apart from this, we also observed a decrease in the magnitude of Pb displacement in PLZST when compared to PZ. In PZ, the dominant Pb displacement is between approximately 45 and 80 pm while it ranges from 20 to 50 pm in PLZST. A significant difference between prototypical and modified systems was reported in lead-free $NaNbO_3$ antiferroelectrics, indicating a suppression of ferroelectricity in the modified system which hence accounts for the stabilized antiferroelectricity.[67]

The ^{207}Pb NMR spectrum of PLZST features only one broad signal with a chemical shift range stretching across the regions of the Pb_1 and Pb_2 site of PZ (Figure 3d). The signal is well described by a single Gaussian line (Figure S5), indicating a single average Pb environment in turn. Based on the width and shape of the signal, it can be concluded that the Pb sites in PLZST exhibit structural disorder in accordance with the disarranged Pb displacement pattern (Figure 3c). In particular, the broadening of the ^{207}Pb 2D-PASS signal along the direct spectral dimension reflects an overlay of spectral lines following a statistical distribution of δ_{iso}. In PZ-based materials, δ_{iso} is strongly influenced by Pb−O bond lengths; hence, a distribution of δ_{iso} reflects the presence of bond length disorder. Compared to the narrow, Lorentzian lines for the two signals of PZ ($FWHM_1$ = 55 ppm and $FWHM_2$ = 66 ppm, Figure 3e), the PLZST signal is approximately 5.7 times wider, exhibiting a FWHM of 342 ppm. We can conclude the following: If Pb_1 and Pb_2 are defined as the Pb atoms located in adjacent layers along the $[001]_p$ direction, the NMR results indicate that these two species are no longer associated with distinct structural features related to Pb displacements or Pb−O bond lengths. Instead, the Pb−O bond lengths in both types of layers are modulated with displacive disorder that

https://doi.org/10.1021/acs.chemmater.3c02045
Chem. Mater. 2023, 35, 10041−10049

exceeds the differences between Pb_1−O and Pb_2−O bond lengths in the original $PbZrO_3$.

The high degree of disorder observed with NMR spectroscopy could potentially indicate a structure that departs from a FE- or AFE-like polarization configuration, both of which require an ordered polarization direction. For example, AFE-to-relaxor phase transitions have previously been reported for PZ-based ceramics.[68] However, our TEM analysis clearly reveals a polarization configuration that may not be fully compensated, but is still directional, indicating that if a departure from the AFE phase is taking place in our sample, it should not be regarded as complete.

It is notable that the average chemical shift (δ_{av}^{iso} = −1248 ± 0.3 ppm) is not located at the arithmetic mean between the Pb_1 and Pb_2 signals from PZ but appears shifted toward the vicinity of Pb_2 instead (Figure 3e). Meanwhile, the signal's CSA is approximately −555 ± 10 ppm at the average position (Figure S6). This value is much closer to that of the Pb_2 site in PZ (CSA_1 = −520 ppm) than that of the Pb_1 site (CSA_2 = −855 ppm). Thus, in spite of the broad distribution of Pb−O bond lengths expected in the material, overall, the Pb atoms favor a Pb_2-like environment.

The capability of ^{207}Pb NMR spectroscopy to detect and measure Pb−O bond length disorder means that our findings can be more directly correlated. We acquire ABF images simultaneously with HAADF images to quantify the Pb−O distance distributions in-plane (planar PbO_4 array). Then, we calculate Pb−O distance distributions within the PbO_{12} coordination spheres, i.e., in-plane and out-of-plane, from the ^{207}Pb NMR spectra to obtain a full, multidimensional picture of Pb displacements in PLZST. The basis of this analysis is the fundamental relationship between the shortest Pb−O bond in a planar PbO_4 array or a 3-dimensional PbO_{12} unit with the displacement of the Pb atom from its center of symmetry, in-plane or out-of-plane. To determine the in-plane contribution, the ABF image is rotated so that the direction of the Pb displacement is perpendicular to the $[110]_p$ direction. This procedure allows a more intuitive understanding of the following calculation and plotting of the Pb−O distances. In the ABF image shown in Figure 4a, three types of contrast are recognized that can be attributed to the atoms occupying the A (Pb), B (Zr), and O sites, respectively. By calculating the distance between Pb and four surrounding O atoms, four Pb−O distances are determined for a series of Pb atomic positions in several atomic layers along the $[1\bar{1}0]_p$ direction, as indicated by the orange arrow in Figure 4a,b. Values obtained for the average and shortest Pb−O distances are then plotted with respect to the atomic column positions along the $[110]_p$ direction of the lattice, as shown in Figure 4c,d. Values of the average Pb−O distance, representing the average of the local environment of Pb, are clustered and found to occur either between 3.1 and 3.4 Å or between 2.5 and 2.8 Å. The average of the collected data is 2.85 Å and is in qualitative agreement with the diffraction values of 2.96−2.92 Å reported for the crystal structure.[38] Meanwhile, the shortest distances, representing a measure of Pb displacement from the high-symmetry position, are distributed between 1.5 and 2.1 Å.

In ^{207}Pb NMR spectroscopy, the presence and extent of bond length disorder in the bulk material can be evaluated based on the signal line widths employing eq 1 as recalled in detail in the Supporting Information.[22,44,59−61] The broad signal in the spectrum of PLZST (δ_{av}^{iso} = −1248 ppm, FWHM = 342 ppm) corresponds to a distribution width of 0.017 Å with an effective Pb−O bond length of 2.55 Å. In comparison, if the widths of the two signals in PZ are fully attributed to a distribution of δ_{iso}, they correspond to a bond length distribution width of only approximately 0.003 Å, i.e., 5−6 times smaller than in PLZST (Figure 4e,f).[59] The effective bond length determined from NMR spectroscopy (2.55 Å) lies between the values for the average (2.85 Å) and shortest (1.5−2.1 Å) in-plane bonds as determined from STEM and is close to the shortest Pb−O bonds in the crystal structure of PZ (2.53−2.57 Å).[38] On a quantitative scale, NMR spectroscopy therefore indicates a smaller variation as seen from HAADF-STEM and is more consistent with the XRD structure reported in the literature.[38] Thus, ^{207}Pb NMR spectroscopy suggests that the overall Pb−O displacement configuration (in-plane and out-of-plane) throughout the bulk sample corresponds more closely to the average crystal structure than expected from the in-plane configuration as seen locally by the STEM characterization. This observation highlights the benefits of combining a short-range method such as STEM with a bulk method such as NMR spectroscopy in order to probe more accurately the distributions of local structural parameters across the sample volume.

Nonetheless, the NMR line width reflects a significant Pb−O bond length distribution. This variation of local environments demonstrates that the bulk structure is disordered on the NMR length scale as well. Specifically, the ^{207}Pb signal of PLZST exhibits Gaussian−rather than Lorentzian−line broadening along the direct dimension of the 2D-PASS spectrum. Zhou et al.[60] have previously shown the Gaussian line shape to be consistent with random disorder of Pb displacement magnitudes along a single, unique direction in PZ-based perovskites and were able to distinguish this type of displacement configuration from a model where Pb atoms are displaced in random directions instead. However, as the isotropic value of the chemical shift tensor is a nondirectional property, it does not provide information about the crystallographic direction(s) along which the displacements occur. The STEM imaging performed in this work revealed disorder of both magnitude and direction, thus potentially challenging the generality of the result reported by Zhou et al. However, we can also interpret these results as indicating that the disorder of displacement magnitudes is the dominant effect *only* when both in-plane and out-of-plane Pb−O distances are considered. Thus, the coalescence of the Pb_1 and Pb_2 sites into a single, highly disordered environment either reflects a disordered out-of-plane component in addition to the in-plane modulation or disorder of the in-plane modulation that is large enough to surpass the differences between adjacent out-of-plane layers.

4. CONCLUSIONS

Atomic-resolution TEM and solid-state NMR spectroscopy were employed in a novel joint approach to probe the configurations of Pb atoms in AFE oxides PZ and PLZST. Our analysis went beyond the in-plane displacements as limited by (S)TEM and made use of NMR's sensitivity to the differences between Pb species to analyze the 3-dimensional structure. In PZ, a well-defined 4-fold modulation of the Pb displacement was confirmed with(S)TEM, which is expected for the alternating displacement configuration of the AFE structure. This was further supported by the two distinct Pb signals in the NMR spectrum, revealing a short-range structure with no indication of significant displacement disorder neither in-plane nor out-of-plane in the bulk sample. In contrast, the modified

https://doi.org/10.1021/acs.chemmater.3c02045
Chem. Mater. 2023, 35, 10041−10049

AFE PLZST demonstrates vigorous inhomogeneity of the modulation, designating a pronounced disorder of the Pb environment. Moreover, a distribution of both the shortest and average Pb−O distance is observed in-plane. This is supplemented by the single ^{207}Pb NMR signal with a broad distribution of isotropic chemical shifts, reflecting a disorder of the displacement magnitudes that is at least 5−6 times larger than observed in PZ. When both in-plane and out-of-plane displacements were considered, a significantly closer correspondence to the crystal structure and a smaller distribution width were found compared to when only in-plane displacements were considered. The introduction of this displacive disorder is accompanied by a favoring of Pb_2-like local structures, highlighting the importance of considering the 3-dimensional structure. The complementary investigation is highly promising for future in-depth structural studies of cation displacements in disordered materials; hence establishing the groundwork for correlating structure and property.

■ ASSOCIATED CONTENT

Supporting Information

The Supporting Information is available free of charge at https://pubs.acs.org/doi/10.1021/acs.chemmater.3c02045.

Supplementary experimental procedures; powder XRD patterns; hysteresis loops; ^{207}Pb 2D-PASS spectrum of commercial PZ; Supplementary HAADF-STEM images of the PZ ceramic; isotropic and anisotropic projections of the ^{207}Pb 2D-PASS spectra; effective Pb−O distance calculation; CSA conventions (PDF)

■ AUTHOR INFORMATION

Corresponding Authors

Hui Ding − *Department of Materials and Earth Sciences, Technical University of Darmstadt, Darmstadt 64287, Germany;* orcid.org/0000-0001-5722-0053; Email: h.ding@mpie.de

Gerd Buntkowsky − *Eduard Zintl Institute for Inorganic and Physical Chemistry, Technical University of Darmstadt, Darmstadt 64287, Germany;* orcid.org/0000-0003-1304-9762; Email: gerd.buntkowsky@chemie.tu-darmstadt.de

Leopoldo Molina-Luna − *Department of Materials and Earth Sciences, Technical University of Darmstadt, Darmstadt 64287, Germany;* orcid.org/0000-0002-9412-8093; Email: leopoldo.molina-luna@aem.tu-darmstadt.de

Sonja Egert − *Eduard Zintl Institute for Inorganic and Physical Chemistry, Technical University of Darmstadt, Darmstadt 64287, Germany;* orcid.org/0000-0001-5876-8766; Email: sie1@st-andrews.ac.uk

Authors

Binxiang Huang − *Department of Materials and Earth Sciences, Technical University of Darmstadt, Darmstadt 64287, Germany;* orcid.org/0000-0002-6449-2847

Tianshu Jiang − *Department of Materials and Earth Sciences, Technical University of Darmstadt, Darmstadt 64287, Germany*

Leif Carstensen − *Department of Materials and Earth Sciences, Technical University of Darmstadt, Darmstadt 64287, Germany*

Edina Šić − *Eduard Zintl Institute for Inorganic and Physical Chemistry, Technical University of Darmstadt, Darmstadt 64287, Germany*

Yucheng Liu − *College of Materials Science and Engineering, Tongji University, Shanghai 201804, China*

Tongqing Yang − *College of Materials Science and Engineering, Tongji University, Shanghai 201804, China*

Pedro Braga Groszewicz − *Department of Radiation Science and Technology, Delft University of Technology, Delft 2629JB, Netherlands*

Hans-Joachim Kleebe − *Department of Materials and Earth Sciences, Technical University of Darmstadt, Darmstadt 64287, Germany*

Andreas Klein − *Department of Materials and Earth Sciences, Technical University of Darmstadt, Darmstadt 64287, Germany*

Complete contact information is available at: https://pubs.acs.org/10.1021/acs.chemmater.3c02045

Author Contributions

H.D. and S.E. contributed equally to this work. H.D. characterized and analyzed the structure using TEM under the supervision of H.-J.K. and L.M.-L. S.E. characterized and analyzed the structure using solid-state NMR spectroscopy under the supervision of G.B. and P.B.G. and in conjunction with E.S. B.-X.H. conceived the idea of the combination of these two methods and synthesized the PLZST sample under the supervision of A.K. Y-L.C. synthesized the PZ sample under the supervision of T.-Q.Y. T.-S.J. helped adapt the Python code for displacement mapping and sublattice plane distance measurement. L.C. provided valuable feedback in terms of the structures based on his XRD characterization. H.D. and S.E. wrote the first version of the manuscript and all authors contributed to its revision and gave approval to the final version of the manuscript.

Notes

The authors declare no competing financial interest.

■ ACKNOWLEDGMENTS

This work was supported by the Hessian State Ministry for Higher Education, Research and the Arts under the LOEWE collaborative project FLAME (Fermi level engineering of antiferroelectric materials for energy storage and insulation systems). P.G. acknowledges financial support by the Dutch Research Council (NWO) for the ECCM Tenure Track funding under project number ECCM.006. G.B. acknowledges financial support by the Deutsche Forschungsgemeinschaft DFG under contract Bu-911/28-2. H.D. acknowledged N.Cautaerts and B. Berkels as developers of the non-rigid registration python package. T.J. and L.M-L. acknowledge funding by the European Research Council (ERC) through the "Horizon 2020" Program under Grant No. 805359-FOXON and 957521-STARE.

■ REFERENCES

(1) Han, X.-B.; Jing, C.-Q.; Zu, H.-Y.; Zhang, W. Structural Descriptors to Correlate Pb Ion Displacement and Broadband Emission in 2D Halide Perovskites. *J. Am. Chem. Soc.* **2022**, *144* (40), 18595−18606.

(2) Laurita, G.; Fabini, D. H.; Stoumpos, C. C.; Kanatzidis, M. G.; Seshadri, R. Chemical Tuning of Dynamic Cation Off-Centering in the Cubic Phases of Hybrid Tin and Lead Halide Perovskites. *Chem. Sci.* **2017**, *8* (8), 5628−5635.

(3) Wang, F.; Grinberg, I.; Rappe, A. M. Band Gap Engineering Strategy Via Polarization Rotation in Perovskite Ferroelectrics. *Appl. Phys. Lett.* **2014**, *104* (15), 152903.
(4) Warren, W. L.; Robertson, J.; Dimos, D.; Tuttle, B. A.; Pike, G. E.; Payne, D. A. Pb Displacements in Pb(Zr, Ti) O_3 Perovskites. *Phys. Rev. B* **1996**, *53* (6), 3080−3087.
(5) Yang, D.; Gao, J.; Shu, L.; Liu, Y.-X.; Yu, J.; Zhang, Y.; Wang, X.; Zhang, B.-P.; Li, J.-F. Lead-Free Antiferroelectric Niobates $AgNbO_3$ and $NaNbO_3$ for Energy Storage Applications. *J. Mater. Chem. A* **2020**, *8* (45), 23724−23737.
(6) Maurya, D.; Pramanick, A.; Feygenson, M.; Neuefeind, J. C.; Bodnar, R. J.; Priya, S. Effect of Poling on Nanodomains and Nanoscale Structure in A-Site Disordered Lead-Free Piezoelectric $Na_{0.5}Bi_{0.5}TiO_3$-$BaTiO_3$. *J. Mater. Chem. C* **2014**, *2* (39), 8423−8431.
(7) Hao, X.; Zhai, J.; Kong, L. B.; Xu, Z. A Comprehensive Review on the Progress of Lead Zirconate-Based Antiferroelectric Materials. *Prog. Mater. Sci.* **2014**, *63*, 1−57.
(8) Wang, H.; Srot, V.; Jiang, X.; Yi, M.; Wang, Y.; Boschker, H.; Merkle, R.; Stark, R. W.; Mannhart, J.; van Aken, P. A. Probing Charge Accumulation at $SrMnO_3$/ $SrTiO_3$ Heterointerfaces via Advanced Electron Microscopy and Spectroscopy. *ACS Nano* **2020**, *14*, 12697.
(9) Wei, X.-K.; Jia, C.-L.; Du, H.-C.; Roleder, K.; Mayer, J.; Dunin-Borkowski, R. E. An Unconventional Transient Phase with Cycloidal Order of Polarization in Energy-Storage Antiferroelectric $PbZrO_3$. *Adv. Mater.* **2020**, *32* (9), 1907208.
(10) MacLaren, I.; Villaurrutia, R.; Schaffer, B.; Houben, L.; Peláiz-Barranco, A. Atomic-Scale Imaging and Quantification of Electrical Polarisation in Incommensurate Antiferroelectric Lanthanum-Doped Lead Zirconate Titanate. *Adv. Funct. Mater.* **2012**, *22* (2), 261−266.
(11) Jia, C.-L.; Nagarajan, V.; He, J.-Q.; Houben, L.; Zhao, T.; Ramesh, R.; Urban, K.; Waser, R. Unit-Cell Scale Mapping of Ferroelectricity and Tetragonality in Epitaxial Ultrathin Ferroelectric Films. *Nat. Mater.* **2007**, *6* (1), 64−69.
(12) Jia, C.-L.; Mi, S.-B.; Urban, K.; Vrejoiu, I.; Alexe, M.; Hesse, D. Atomic-Scale Study of Electric Dipoles near Charged and Uncharged Domain Walls in Ferroelectric Films. *Nat. Mater.* **2008**, *7* (1), 57−61.
(13) Keen, D. A.; Goodwin, A. L. The Crystallography of Correlated Disorder. *Nature* **2015**, *521* (7552), 303−309.
(14) Koruza, J.; Groszewicz, P.; Breitzke, H.; Buntkowsky, G.; Rojac, T.; Malič, B. Grain-Size-Induced Ferroelectricity in $NaNbO_3$. *Acta Mater.* **2017**, *126*, 77−85.
(15) Höfling, M.; Zhou, X.; Riemer, L. M.; Bruder, E.; Liu, B.; Zhou, L.; Groszewicz, P. B.; Zhuo, F.; Xu, B.-X.; Durst, K.; Tan, X.; Damjanovic, D.; Koruza, J.; Rödel, J. Control of Polarization in Bulk Ferroelectrics by Mechanical Dislocation Imprint. *Science* **2021**, *372* (6545), 961−964.
(16) Johnston, K. E.; Tang, C. C.; Parker, J. E.; Knight, K. S.; Lightfoot, P.; Ashbrook, S. E. The Polar Phase of $NaNbO_3$: A Combined Study by Powder Diffraction, Solid-State NMR, and First-Principles Calculations. *J. Am. Chem. Soc.* **2010**, *132* (25), 8732−8746.
(17) Ashbrook, S. E.; Le Polles, L.; Gautier, R.; Pickard, C. J.; Walton, R. I. ^{23}Na Multiple-Quantum MAS NMR of the Perovskites $NaNbO_3$ and $NaTaO_3$. *Phys. Chem. Chem. Phys.* **2006**, *8* (29), 3423−3431.
(18) Egert, S.; Zhang, M.-H.; Koruza, J.; Groszewicz, P. B.; Buntkowsky, G. ^{23}Na NMR Spectroscopic Quantification of the Antiferroelectric-Ferroelectric Phase Coexistence in Sodium Niobate. *J. Phys. Chem. C* **2020**, *124* (43), 23852−23858.
(19) Zhang, M.-H.; Fulanović, L.; Egert, S.; Ding, H.; Groszewicz, P. B.; Kleebe, H.-J.; Molina-Luna, L.; Koruza, J. Electric-Field-Induced Antiferroelectric to Ferroelectric Phase Transition in Polycrystalline $NaNbO_3$. *Acta Mater.* **2020**, *200*, 127−135.
(20) Zhang, M.-H.; Ding, H.; Egert, S.; Zhao, C.; Villa, L.; Fulanović, L.; Groszewicz, P. B.; Buntkowsky, G.; Kleebe, H.-J.; Albe, K.; Klein, A.; Koruza, J. Tailoring High-Energy Storage $NaNbO_3$-Based Materials from Antiferroelectric to Relaxor States. *Nat. Commun.* **2023**, *14* (1), 1525.
(21) Hoatson, G. L.; Zhou, D. H.; Fayon, F.; Massiot, D.; Vold, R. L. ^{93}Nb Magic Angle Spinning NMR Study of Perovskite Relaxor Ferroelectrics (1-x) $Pb(Mg_{1/3}Nb_{2/3})$ O_3-$xPbSc_{1/2}Nb_{1/2}O_3$. *Phys. Rev. B* **2002**, *66* (22), 224103.
(22) Zhou, D. H.; Hoatson, G. L.; Vold, R. L.; Fayon, F. Local Structure in Perovskite Relaxor Ferroelectrics by ^{207}Pb NMR. *Phys. Rev. B* **2004**, *69* (13), 134104.
(23) Laguta, V. V.; Glinchuk, M. D.; Bykov, I. P.; Blinc, R.; Zalar, B. NMR Study of Ionic Shifts and Polar Ordering in the Relaxor Ferroelectric $PbSc_{1/2}Nb_{1/2}O_3$. *Phys. Rev. B* **2004**, *69* (5), 054103.
(24) Groszewicz, P. B.; Gröting, M.; Breitzke, H.; Jo, W.; Albe, K.; Buntkowsky, G.; Rödel, J. Reconciling Local Structure Disorder and the Relaxor State in $(Bi_{1/2}Na_{1/2})$ TiO_3-$BaTiO_3$. *Sci. Rep* **2016**, *6* (1), 31739.
(25) Veerapandiyan, V.; Popov, M. N.; Mayer, F.; Spitaler, J.; Svirskas, S.; Kalendra, V.; Lins, J.; Canu, G.; Buscaglia, M. T.; Pasciak, M.; Banys, J.; Groszewicz, P. B.; Buscaglia, V.; Hlinka, J.; Deluca, M. Origin of Relaxor Behavior in Barium-Titanate-Based Lead-Free Perovskites. *Adv. Electron. Mater.* **2022**, *8* (2), 2100812.
(26) Zhang, M.-H.; Hadaeghi, N.; Egert, S.; Ding, H.; Zhang, H.; Groszewicz, P. B.; Buntkowsky, G.; Klein, A.; Koruza, J. Design of Lead-Free Antiferroelectric (1-x) $NaNbO_3$-$x$$SrSnO_3$ Compositions Guided by First-Principles Calculations. *Chem. Mater.* **2021**, *33* (1), 266−274.
(27) Ashbrook, S. E.; McKay, D. Combining Solid-State NMR Spectroscopy with First-Principles Calculations - a Guide to NMR Crystallography. *Chem. Commun.* **2016**, *52* (45), 7186−7204.
(28) Liu, Z.; Lu, T.; Ye, J.; Wang, G.; Dong, X.; Withers, R.; Liu, Y. Antiferroelectrics for Energy Storage Applications: A Review. *Adv. Mater. Technol.* **2018**, *3* (9), 1800111.
(29) Randall, C. A.; Fan, Z.; Reaney, I.; Chen, L.-Q.; Trolier-McKinstry, S. Antiferroelectrics: History, Fundamentals, Crystal Chemistry, Crystal Structures, Size Effects, and Applications. *J. Am. Ceram. Soc.* **2021**, *104* (8), 3775−3810.
(30) Mischenko, A. S.; Zhang, Q.; Scott, J. F.; Whatmore, R. W.; Mathur, N. D. Giant Electrocaloric Effect in Thin-Film $PbZr_{0.95}Ti_{0.05}O_3$. *Science* **2006**, *311* (5765), 1270−1271.
(31) Novak, N.; Weyland, F.; Patel, S.; Guo, H.; Tan, X.; Rödel, J.; Koruza, J. Interplay of Conventional with Inverse Electrocaloric Response in (Pb, Nb) (Zr, Sn, Ti) O_3 Antiferroelectric Materials. *Phys. Rev. B* **2018**, *97* (9), 094113.
(32) Yadav, A. K.; Nelson, C. T.; Hsu, S. L.; Hong, Z.; Clarkson, J. D.; Schlepütz, C. M.; Damodaran, A. R.; Shafer, P.; Arenholz, E.; Dedon, L. R.; Chen, D.; Vishwanath, A.; Minor, A. M.; Chen, L. Q.; Scott, J. F.; Martin, L. W.; Ramesh, R. Observation of Polar Vortices in Oxide Superlattices. *Nature* **2016**, *530* (7589), 198−201.
(33) Fu, Z.; Chen, X.; Li, Z.; Hu, T.; Zhang, L.; Lu, P.; Zhang, S.; Wang, G.; Dong, X.; Xu, F. Unveiling the Ferrielectric Nature of $PbZrO_3$-Based Antiferroelectric Materials. *Nat. Commun.* **2020**, *11* (1), 3809.
(34) Ma, T.; Fan, Z.; Xu, B.; Kim, T.-H.; Lu, P.; Bellaiche, L.; Kramer, M. J.; Tan, X.; Zhou, L. Uncompensated Polarization in Incommensurate Modulations of Perovskite Antiferroelectrics. *Phys. Rev. Lett.* **2019**, *123* (21), 217602.
(35) Ma, T.; Fan, Z.; Tan, X.; Zhou, L. Atomically Resolved Domain Boundary Structure in Lead Zirconate-Based Antiferroelectrics. *Appl. Phys. Lett.* **2019**, *115* (12), 122902.
(36) Wei, X.-K.; Tagantsev, A. K.; Kvasov, A.; Roleder, K.; Jia, C.-L.; Setter, N. Ferroelectric Translational Antiphase Boundaries in Nonpolar Materials. *Nat. Commun.* **2014**, *5* (1), 3031.
(37) Wei, X.-K.; Jia, C.-L.; Roleder, K.; Dunin-Borkowski, R. E.; Mayer, J. In Situ Observation of Point-Defect-Induced Unit-Cell-Wise Energy Storage Pathway in Antiferroelectric $PbZrO_3$. *Adv. Func Mater.* **2021**, *31*, 2008609.
(38) Corker, D. L.; Glazer, A. M.; Dec, J.; Roleder, K.; Whatmore, R. W. A Re-Investigation of the Crystal Structure of the Perovskite $PbZrO_3$ by X-Ray and Neutron Diffraction. *Acta Crystallogr. B Struct. Sci.* **1997**, *53* (1), 135−142.

(39) Kuroiwa, Y.; Terado, Y.; Moriyoshi, C. Electron Charge Density Study on Antiferroelectric Phase Transition in $PbZrO_3$. *Ferroelectrics* **2007**, *354* (1), 158−166.
(40) Vogt, F. G.; Gibson, J. M.; Aurentz, D. J.; Mueller, K. T.; Benesi, A. J. Multiple-Rotor-Cycle 2D PASS Experiments with Applications to ^{207}Pb NMR Spectroscopy. *J. Magn. Reson.* **2000**, *143* (1), 153−160.
(41) Van Bramer, S. E.; Glatfelter, A.; Bai, S.; Dybowski, C.; Neue, G.; Perry, D. L. Solid-State ^{207}Pb NMR Studies of Lead-Group 16 and Mixed Transition-Metal/Lead-Group 16 Element-Containing Materials. *Magn. Reson. Chem.* **2006**, *44* (3), 357−365.
(42) Bykov, I. P.; Zagorodniy, Y. A.; Yurchenko, L. P.; Korduban, A. M.; Nejezchleb, K.; Trachevsky, V. V.; Dimza, V.; Jastrabik, L.; Dejneka, A. Using the Methods of Radiospectroscopy (EPR, NMR) to Study the Nature of the Defect Structure of Solid Solutions Based on Lead Zirconate Titanate (PZT). *IEEE Trans Ultrason Ferroelectr Freq Control* **2014**, *61* (8), 1379−1385.
(43) Antzutkin, O. N.; Shekar, S. C.; Levitt, M. H. Two-Dimensional Sideband Separation in Magic-Angle-Spinning NMR. *J. Magn. Reson.* **1995**, *115*, 7−19.
(44) Egert, S.; Koruza, J.; Breitzke, H.; Zhao, C.; Malic, B.; Buntkowsky, G.; Groszewicz, P. B. Fundamental Workings of Chemical Substitution at the A-Site of Perovskite Oxides— a ^{207}Pb NMR Study of Ba-Substituted $PbZrO_3$. *Dalton Trans.* **2022**, *51* (46), 17827−17835.
(45) Wang, H.; Liu, Y.; Yang, T.; Zhang, S. Ultrahigh Energy-Storage Density in Antiferroelectric Ceramics with Field-Induced Multiphase Transitions. *Adv. Funct. Mater.* **2019**, *29* (7), 1807321.
(46) Ding, H.; Zhang, M.-H.; Koruza, J.; Molina-Luna, L.; Kleebe, H.-J. Domain Morphology of Newly Designed Lead-Free Antiferroelectric $NaNbO_3$-$SrSnO_3$ Ceramics. *J. Am. Ceram. Soc.* **2021**, *104* (7), 3715−3725.
(47) Nord, M.; Vullum, P. E.; MacLaren, I.; Tybell, T.; Holmestad, R. Atomap: A New Software Tool for the Automated Analysis of Atomic Resolution Images Using Two-Dimensional Gaussian Fitting. *Adv. Struct. Chem. Imag* **2017**, *3* (1), 9.
(48) Eoghan, O.; Michael, H.; Eoin, M. PinkShnack/TEMUL. DOI: 10.5281/zenodo.4543963.
(49) Fayon, F.; Bessada, C.; Douy, A.; Massiot, D. Chemical Bonding of Lead in Glasses through Isotropic vs Anisotropic Correlation: PASS Shifted Echo. *J. Magn. Reson.* **1999**, *137* (1), 116−121.
(50) Antzutkin, O. N.; Shekar, S. C.; Levitt, M. H. Two-Dimensional Sideband Separation in Magic-Angle-Spinning NMR. *J. Magn. Reson.* **1995**, *115* (1), 7−19.
(51) Zhao, P.; Prasad, S.; Huang, J.; Fitzgerald, J. J.; Shore, J. S. Lead-207 NMR Spectroscopic Study of Lead-Based Electronic Materials and Related Lead Oxides. *J. Phys. Chem. B* **1999**, *103* (48), 10617−10626.
(52) Massiot, D.; Fayon, F.; Capron, M.; King, I.; Le Calvé, S.; Alonso, B.; Durand, J.-O.; Bujoli, B.; Gan, Z.; Hoatson, G. Modelling One- and Two-Dimensional Solid-State NMR Spectra. *Magn. Reson. Chem.* **2002**, *40* (1), 70−76.
(53) Zhang, N.; Yokota, H.; Glazer, A. M.; Thomas, P. A. Neutron Powder Diffraction Refinement of $PbZr_{(1-x)}Ti_xO_3$. *Acta Cryst. B* **2011**, *67* (5), 386−398.
(54) Kittel, C. Theory of Antiferroelectric Crystals. *Phys. Rev.* **1951**, *82* (5), 729−732.
(55) Zhang, L.; Fu, Z.; Chen, X.; Li, Z.; Hu, T.; Yu, Z.; Wang, G.; Dong, X.; Xu, F. Chemically Tunable Textured Interfacial Defects in $PbZrO_3$-Based Antiferroelectric Perovskite Oxides. *Chem. Mater.* **2021**, *33* (17), 6743−6751.
(56) Liu, H.; Zhou, Z.; Qiu, Y.; Gao, B.; Sun, S.; Lin, K.; Ding, L.; Li, Q.; Cao, Y.; Ren, Y.; Sun, J.; Xing, X.; Chen, J. An Intriguing Intermediate State as a Bridge between Antiferroelectric and Ferroelectric Perovskites. *Mater. Horiz.* **2020**, *7* (7), 1912−1918.
(57) Yao, Y.; Naden, A.; Tian, M.; Lisenkov, S.; Beller, Z.; Kumar, A.; Kacher, J.; Ponomareva, I.; Bassiri-Gharb, N. Ferrielectricity in the Archetypal Antiferroelectric, $PbZrO_3$. *Adv. Mater.* **2023**, *35* (3), 2206541.
(58) Rabe, K. M. Antiferroelectricity in Oxides: A Reexamination. In *Functional Metal Oxides*; Ogale, S. B., Venkatesan, T. V., Blamire, M. G., Eds.; Wiley-VCH Verlag GmbH & Co. KGaA: Weinheim, Germany, 2013; pp 221−244.
(59) Fayon, F.; Farnan, I.; Bessada, C.; Coutures, J.; Massiot, D.; Coutures, J. P. Empirical Correlations between ^{207}Pb NMR Chemical Shifts and Structure in Solids. *J. Am. Chem. Soc.* **1997**, *119* (29), 6837−6843.
(60) Zhou, X. W.; Wadley, H. N. G.; Filhol, J.-S.; Neurock, M. N. Modified Charge Transfer-Embedded Atom Method Potential for Metal/Metal Oxide Systems. *Phys. Rev. B* **2004**, *69* (3), 035402.
(61) Avalos, C. E.; Walder, B. J.; Emsley, L. Lead-Oxygen Bond Length Distributions of the Relaxor Ferroelectric $0.67Pb(Mg_{1/3}Nb_{2/3})O_3$-$0.33PbTiO_3$ from ^{207}Pb Nuclear Magnetic Resonance. *J. Phys. Chem. C* **2019**, *123* (25), 15744−15750.
(62) Teslic, S.; Egami, T.; Viehland, D. Structural Instabilities in PZT. *Ferroelectrics* **1997**, *194* (1), 271−285.
(63) Teslic, S.; Egami, T. Atomic Structure of $PbZrO_3$ Determined by Pulsed Neutron Diffraction. *Acta Cryst. B* **1998**, *54* (6), 750−765.
(64) Korniyenko, S. M.; Bykov, I. P.; Glinchuk, M. D.; Laguta, V. V.; Jastrabik, L. Structure of Lead Zirconium Oxide: Evidence from NMR. *Eur. Phys. J. AP* **1999**, *7* (1), 13−17.
(65) Asada, T.; Koyama, Y. La-Induced Conversion Between the Ferroelectric and Antiferroelectric Incommensurate Phases in $Pb_{(1-x)}La_x(Zr_{(1-y)}Ti_y)O_3$. *Phys. Rev. B* **2004**, *69* (10), 104108.
(66) He, H.; Tan, X. Electric-Field-Induced Transformation of Incommensurate Modulations in Antiferroelectric PNZST. *Phys. Rev. B* **2005**, *72* (2), 024102.
(67) Luo, N.; Ma, L.; Luo, G.; Xu, C.; Rao, L.; Chen, Z.; Cen, Z.; Feng, Q.; Chen, X.; Toyohisa, F.; Zhu, Y.; Hong, J.; Li, J.-F.; Zhang, S. Well-Defined Double Hysteresis Loop in NaNbO3 Antiferroelectrics. *Nat. Commun.* **2023**, *14* (1), 1776.
(68) Li, B.; Liu, Q.-X.; Tang, X.-G.; Zhang, T.-F.; Jiang, Y.-P.; Li, W.-H.; Luo, J. Antiferroelectric to Relaxor Ferroelectric Phase Transition in PbO Modified $(Pb_{0.97}La_{0.02})(Zr_{0.95}Ti_{0.05})O_3$ Ceramics with a Large Energy-Density for Dielectric Energy Storage. *RSC Adv.* **2017**, *7* (68), 43327−43333.

https://doi.org/10.1021/acs.chemmater.3c02045
Chem. Mater. 2023, 35, 10041−10049